

Article

Simultaneous Dirac-like Cones at Two Energy States in Tunable Phononic Crystals: An Analytical and Numerical Study

Mustahseen M. Indaleeb  and Sourav Banerjee * 

Integrated Material Assessment & Predictive Simulations Laboratory (iMAPS), Department of Mechanical Engineering, University of South Carolina, Columbia, SC 29208, USA; indaleeb@email.sc.edu

* Correspondence: banerjes@cec.sc.edu

Abstract: Simultaneous occurrence of Dirac-like cones at the center of the Brillouin zone (Γ) at two different energy states is termed Dual-Dirac-like cones (DDC) in this article. The occurrence of DDC is a rare phenomenon. Thus, the generation of multiple Dirac-like cones at the center of the Brillouin zone is usually non-manipulative and poses a challenge to achieve through traditional accidental degeneracy. However, if predictively created, DDC will have multiple engineering applications with acoustics and vibration. Thus, the possibilities of creating DDC have been identified herein using a simple square periodic array of tunable square phononic crystals (PnCs) in air media. It was found that antisymmetric deaf bands may play critical roles in tracking the DDC. Hence, pivoting on the deaf bands at two different energy states, an optimized tuning parameter was found to achieve Dirac-like cones at two distinct frequency states, simultaneously. Orthogonal wave transport identified as key Dirac phenomena was achieved at two frequencies, herein. It was identified that beyond the Dirac-like cone, the Dirac phenomena remain dominant when a doubly degenerated state created by a top band with positive curvature and a near-flat deaf band are lifted from a bottom band with negative curvature. Utilizing a mechanism of rotating the PnCs near a fixed deaf band, frequencies are tracked to form the DDC, and orthogonal wave transport is demonstrated. Exploiting the dispersion behavior, unique acoustic phenomena, such as ballistic wave transmission, pseudo diffusion and acoustic cloaking are also demonstrated at the Dirac frequencies using numerical simulation. The proposed tunable acoustic PnCs will have important applications in acoustic and ultrasonic imaging, waveguiding and even acoustic computing.



Citation: Indaleeb, M.M.; Banerjee, S. Simultaneous Dirac-like Cones at Two Energy States in Tunable Phononic Crystals: An Analytical and Numerical Study. *Crystals* **2021**, *11*, 1528. <https://doi.org/10.3390/cryst11121528>

Academic Editors: Jin-Chen Hsu and Jia-Hong Sun

Received: 9 November 2021

Accepted: 6 December 2021

Published: 7 December 2021

Publisher's Note: MDPI stays neutral with regard to jurisdictional claims in published maps and institutional affiliations.



Copyright: © 2021 by the authors. Licensee MDPI, Basel, Switzerland. This article is an open access article distributed under the terms and conditions of the Creative Commons Attribution (CC BY) license (<https://creativecommons.org/licenses/by/4.0/>).

Keywords: phononic crystals; Dirac cone; Dirac-like cone; deaf band; degeneracy; double-Dirac cone; accidental degeneracy; metamaterial

1. Introduction

Phononic crystals (PnCs) are an elastic hetero structure with different elastic properties that has created a new direction of research in acoustic and elastic wave propagation. Wave phenomena in PnCs are extensively studied, with numerous potential applications utilizing the physical understanding of the periodic media [1–7]. Prohibition of certain elastic/acoustic vibrations near bandgaps is one of the prime applications of PnCs, which ultimately helped to understand the Anderson localization [8–10]. Acoustic/elastic isolators, noise filter/control, design of innovative transducers and waveguides have potential applications in biomedical and sensing applications.

Numerous approaches are described in the literature to control the width of the bandgaps by placing tunable phononic crystals at well-defined places. Waveguiding was manipulated by reducing the symmetry of the crystals. Symmetry breaking helped remove the band degeneracies, allowing directional bandgaps [11–15]. However, at any high-symmetry points, accidental threefold-degenerated Bloch mode yields Dirac-like cones. Multifold degeneracy may occur due to periodic symmetry of the hard inclusions when hosted in a matrix. This phenomenon has been meticulously reported at the edge of the

Brillouin zone (BZ). This is popularly known as the topological edge effect or quantum valley Hall effect (QVHE). QVHE was demonstrated through many structures [16–19]. However, generating such phenomena at the center of the BZ is challenging because the periodic insertions reshape the spectral responses, especially when their elastic density is very high compared to other constituents. This phenomenon often occurs in solid inclusions in a fluid matrix.

Artificial increases of the acoustic bandgaps were reported by removing band degeneracies. This was achieved by doubly or triply degenerated bands to maneuver the spectral responses. However, the same process to engineer the double-Dirac cones is rare. Apart from the rigid cylinders in fluid media, [6,11,13,20–22], various geometrical unit shapes with different lattices were studied. Correlations between the lattice symmetry and complete acoustic bandgaps [9,10,23,24] were reported. Tunable PnCs were used to lift or move certain bands. Such band movement increased the bandgaps. Square inclusion in air medium was reported to find complete acoustic bandgaps. Tuning of the square PnCs [20] is reported multiple times, especially for widening the complete acoustic bandgaps by decoupling the degenerated states. Such tuning was achieved by rotating the rods with respect to their initial lattice orientation. Using square inclusion in the air matrix, tuning techniques are reported primarily to break the degeneracy and yield the bandgaps [8,9,25–29].

Unlike bandgaps, the predictability of the Dirac-like phenomena is challenging. The triple degeneration due to accidental degeneracies makes it difficult to propose a predictive design method. However, it is shown that exploiting a similar square geometric tuning, more than one triply degenerated points, i.e., Dual-Dirac-like cones reported herein were not reported earlier. Defying a convenient way, deaf band-based tuning is demonstrated in this article to obtain multiple Dirac-like points at two different energy states. Recently, a deaf band-based predictive model was proposed to control the Dirac-cones [30], which is exploited in this article.

Dirac-like cones, which only occur at the center of the BZ (Γ point), contain double and single degenerated states, forming a triple degeneracy. Triple degeneracy shows linear dispersion at $\vec{k} = 0$. Among three of the degenerated bands, a flat band passes through the degenerated point, having zero or minimal group velocity. Due to near flatness and having no group velocity, it exhibits spatial localization, allowing minimum to no acoustic energy transported through the PnCs. Due to the non-transporting acoustical deafness behavior, the band is called a “deaf band”. The deaf band plays a major role in increasing and reducing the bandgaps above or below the respective bands and helps to form degeneration from non-degenerate modes. Due to an antisymmetric acoustic mode shape with respect to the direction of incidence of the plane wave, it can only be excited with the incidence of nonzero k -parallel components [31–35]. The tuning techniques proposed by the researchers, including authors, require total replacement of the PnCs due to the change in the geometrical dimension. However, in this article, a deaf band-based predictive modeling and tuning technique are proposed, where replacement of the inclusions is not necessary. This helps avoid the process of shape optimization. Instead of cylindrical inclusion, square-section rods hosted in the air are distributed in a square lattice arrangement. The tuning technique proposed is based on a rotating mechanism.

In this article, the tunable dependency between acoustic deaf band modes and rotation of the solid square rod with respect to the lattice orientation is studied. An orthogonal guiding of the elastic waves through PnCs near Dirac frequencies were observed to confirm the emergence of a Dual-Dirac cone at the center of the BZ. Simultaneous occurrence of Dirac-like cones at the center of the Brillouin zone (Γ) at two different energy states is termed Dual-Dirac-like cones (DDC) in this article. The method of finding the band structure for composite media and numerical models is briefly reported in Section 2. The numerical results are discussed in Section 3 and concluded with prime findings in Section 4.

2. Method and Numerical Model Formulation

In solid/fluid mixed media, the coupling of transverse and longitudinal modes is inevitable due to inhomogeneous elastic constants of the constituents. Pure transverse mode propagates along the normal axis and is completely independent of the coupled modes (longitudinal) propagating through PnCs along the plane [36] of the incidence. In this article, square PnCs in air media are considered and plane-wave expansion (PWE) is used [37,38]. The governing wave motion equation for the longitudinal wave modes in solid–fluid media is expressed as

$$\sigma_{ij,j}(x_k) + f_i = \rho(x_k)\ddot{u}_i \quad (1)$$

where i , j and k are the index notation with values 1 and 2 considering the 2D cross-sectional plane of PnCs, $\sigma_{ij,j}(x_k)$ is the derivative of the stresses at location x_k with respect to the j th direction, f_i is the body force in the i th direction, $\rho(x_k)$ is the density at location x_k in the material, and \ddot{u}_i is the acceleration in the i th direction.

The Bloch–Floquet periodic boundary conditions [39] are then applied in the reciprocal wave number space. $G_1 = 2\pi m/D_1$ and $G_2 = 2\pi n/D_2$ are real values of the periodic wave numbers or Bloch wave numbers (where $m = -\infty$ to $+\infty$ and $n = -\infty$ to $+\infty$ using only integers) added with the eigen wave number to obtain the Bloch–Floquet displacement function. D_i is the periodicity of the media in the i th direction. If the wave number \mathbf{k} in Equations (2) and (3) is a solution of the system at a certain frequency ω , then $\mathbf{k} + \mathbf{G}$ is also a solution of the system at the same frequency. The Bloch–Floquet displacement function is expressed as

$$u_1(x_k, t) = \sum_m \sum_n A_{mn} e^{i\mathbf{k}\cdot\mathbf{x}} e^{i\mathbf{G}\cdot\mathbf{x}} e^{-i\omega t} \quad (2)$$

$$u_2(x_k, t) = \sum_m \sum_n B_{mn} e^{i\mathbf{k}\cdot\mathbf{x}} e^{i\mathbf{G}\cdot\mathbf{x}} e^{-i\omega t}, \quad (3)$$

where $\mathbf{G} = G_i \hat{e}_i$ and \hat{e}_i are the Cartesian basis vectors and $\mathbf{G}\cdot\mathbf{x} = G_k x_k$ is the dot product between the reciprocal Bloch wave number and position vector. Similarly, differentiating the displacement function twice with respect to time, the acceleration is

$$\ddot{u}_1(x_k, t) = -\omega^2 \sum_m \sum_n A_{mn} e^{i(\mathbf{k}+\mathbf{G})\cdot\mathbf{x}} e^{-i\omega t} \quad (4)$$

$$\ddot{u}_2(x_k, t) = -\omega^2 \sum_m \sum_n B_{mn} e^{i(\mathbf{k}+\mathbf{G})\cdot\mathbf{x}} e^{-i\omega t} \quad (5)$$

The expressions in Equations (2)–(5) signify the summations over a range of integer values of m and n . In continuum mechanics, the stresses in Equation (1) are further expressed as a product of the constitutive properties of the medium and strain tensor. The strain tensor can be further expressed by the derivative of the displacement functions (Equations (2) and (3)) with respect to the spatial domain x_k . Within an array of PnCs, the constitutive matrix can be assumed to be the periodic function of the space, and respective Fourier coefficients can be found. Hence, applying the Fourier transform of the constitutive function $C_{ij}(x)$, the Fourier coefficients C_{ij}^{pq} can be expressed as

$$C_{ij}(x_k) = \sum_{p=-\infty}^{\infty} \sum_{q=-\infty}^{\infty} C_{ij}^{pq} e^{i(\frac{2\pi p}{D_1} x_1 + \frac{2\pi q}{D_2} x_2)} = \sum \sum C_{ij}^{pq} e^{i\mathbf{G}\cdot\mathbf{x}} \quad (6)$$

where $p = -\infty$ to $+\infty$ and $q = -\infty$ to $+\infty$ use integer values. The derivative of the constitutive function with respect to space x_l is expressed as

$$\frac{\partial C_{ij}(x_k)}{\partial x_l} = (-1)^{l+1} \sum \sum i C_{ij}^{pq} \frac{2\pi(p(2-l) + q(1-l))}{D_l} e^{i\mathbf{G}\cdot\mathbf{x}} \quad (7)$$

where l is also an index with values 1 and 2.

The Fourier coefficients of the constitutive properties are

$$C_{ij}^{pq} = \frac{1}{A_c} \int C_{ij}(x_k) e^{-i\mathbf{G}\cdot\mathbf{x}} d\mathbf{x} \quad (8)$$

Similarly, the Fourier coefficients of the density $\rho(x_k)$ are expressed as

$$\rho^{pq} = \frac{1}{A_c} \int \rho(x_k) e^{-i\mathbf{G}\cdot\mathbf{x}} d\mathbf{x} \quad (9)$$

A generalized expression for the modulus and/or density is thus expressed as

$$\alpha^{pq} = \frac{1}{A_c} \int \alpha(x_k) e^{-i\mathbf{G}\cdot\mathbf{x}} d\mathbf{x} \quad (10)$$

where $\alpha(x_k)$ is equivalent to $C_{ij}(x_k)$ or $\rho(x_k)$.

Substituting Equation (8) into Equation (7) and then substituting Equations (7) and (8) into Equation (1), two governing equations are obtained in a generalized form:

$$\begin{aligned} \sum_m \sum_n \sum_p \sum_q & \left[A_{mn} C_{11}^{pq} e^{i(\mathbf{k}+\mathbf{G}_{pq}+\mathbf{G}_{mn})\cdot\mathbf{x}} \left(k_1 + \frac{2\pi m}{D_1} \right) \left[-k_1 - \frac{2\pi m}{D_1} - \frac{2\pi p}{D_1} \right] \right. \\ & + \frac{1}{2} A_{mn} C_{66}^{pq} e^{i(\mathbf{k}+\mathbf{G}_{pq}+\mathbf{G}_{mn})\cdot\mathbf{x}} \left(k_2 + \frac{2\pi n}{D_2} \right) \left[-k_2 - \frac{2\pi n}{D_2} - \frac{2\pi q}{D_2} \right] \\ & + B_{mn} C_{12}^{pq} e^{i(\mathbf{k}+\mathbf{G}_{pq}+\mathbf{G}_{mn})\cdot\mathbf{x}} \left(k_2 + \frac{2\pi n}{D_2} \right) \left[-k_1 - \frac{2\pi m}{D_1} - \frac{2\pi p}{D_1} \right] \\ & \left. + \frac{1}{2} B_{mn} C_{66}^{pq} e^{i(\mathbf{k}+\mathbf{G}_{pq}+\mathbf{G}_{mn})\cdot\mathbf{x}} \left(k_1 + \frac{2\pi m}{D_1} \right) \left[-k_2 - \frac{2\pi n}{D_2} - \frac{2\pi q}{D_2} \right] \right] \\ & = -\omega^2 \sum_m \sum_n \sum_p \sum_q A_{mn} \rho^{pq} e^{i(\mathbf{k}+\mathbf{G}_{pq}+\mathbf{G}_{mn})\cdot\mathbf{x}} \end{aligned} \quad (11)$$

$$\begin{aligned} \sum_m \sum_n \sum_p \sum_q & \left[A_{mn} C_{21}^{pq} e^{i(\mathbf{k}+\mathbf{G}_{pq}+\mathbf{G}_{mn})\cdot\mathbf{x}} \left(k_1 + \frac{2\pi m}{D_1} \right) \left[-k_2 - \frac{2\pi n}{D_2} - \frac{2\pi q}{D_2} \right] \right. \\ & + \frac{1}{2} A_{mn} C_{66}^{pq} e^{i(\mathbf{k}+\mathbf{G}_{pq}+\mathbf{G}_{mn})\cdot\mathbf{x}} \left(k_2 + \frac{2\pi n}{D_2} \right) \left[-k_1 - \frac{2\pi m}{D_1} - \frac{2\pi p}{D_1} \right] \\ & + B_{mn} C_{22}^{pq} e^{i(\mathbf{k}+\mathbf{G}_{pq}+\mathbf{G}_{mn})\cdot\mathbf{x}} \left(k_2 + \frac{2\pi n}{D_2} \right) \left[-k_2 - \frac{2\pi n}{D_2} - \frac{2\pi q}{D_2} \right] \\ & \left. + \frac{1}{2} B_{mn} C_{66}^{pq} e^{i(\mathbf{k}+\mathbf{G}_{pq}+\mathbf{G}_{mn})\cdot\mathbf{x}} \left(k_1 + \frac{2\pi m}{D_1} \right) \left[-k_1 - \frac{2\pi m}{D_1} - \frac{2\pi p}{D_1} \right] \right] \\ & = -\omega^2 \sum_m \sum_n \sum_p \sum_q B_{mn} \rho^{pq} e^{i(\mathbf{k}+\mathbf{G}_{pq}+\mathbf{G}_{mn})\cdot\mathbf{x}}, \end{aligned} \quad (12)$$

where $\mathbf{k} = k_1 \hat{e}_1 + k_2 \hat{e}_2$, $\mathbf{x} = x_1 \hat{e}_1 + x_2 \hat{e}_2$, $\mathbf{G}_{pq} = \frac{2\pi p}{D_1} \hat{e}_1 + \frac{2\pi q}{D_2} \hat{e}_2$, and $\mathbf{G}_{mn} = \frac{2\pi m}{D_1} \hat{e}_1 + \frac{2\pi n}{D_2} \hat{e}_2$.

For square PnCs with dimension b in an air matrix with equal periodicity $D_1 = D_2 = a$ in both directions, the Fourier coefficients are expressed as

$$\alpha^{mn} = \frac{4\alpha_{sq}}{a^2 G_1 G_2} \sin\left(\frac{G_1 b}{2}\right) \sin\left(\frac{G_2 b}{2}\right), \quad (13)$$

where α_{sq} is the numerical value of the respective property (modulus or density) of a square PnC. Equation (13) is proposed to tune the Bloch modes to obtain the Dual-Dirac-like cones at the Γ point in the Brillouin zone. Hence, by rotating the square rod at an angle θ , the reciprocal lattice vectors following Equation (A14) G_1' and G_2' in the transformed system can be written as

$$G_1' = \frac{2\pi}{a} (m \cos \theta + n \sin \theta) \quad G_2' = \frac{2\pi}{a} (-m \sin \theta + n \cos \theta), \quad (14)$$

where m and n are the integers defined earlier, and a is the lattice constant defined. Hence, due to the rotation of the square PnCs, both \mathbf{G}_{pq}' and \mathbf{G}_{mn}' are transformed with their

respective integers and are substituted in Equations (11) and (12). Equations (11) and (12) together create an eigenvalue problem and at given frequency ω , \mathbf{k} will solve the system of the equations. The solution in the $k - \omega$ domain is the dispersion solution. To obtain the converged dispersion relationship using the PWE on the periodic media, the eigen analysis was conducted with 625 reciprocal vectors, which was adequate when m and n were -12 to 12 [40].

3. Results and Discussion

First, an isolated polyvinyl chloride (PVC) square rod in an air medium is investigated. PVC rods are perfectly rigid, and sound propagation is assumed to be prohibited through the solid constituents. In-plane wave is assumed as having no out-of-plane displacement components. Hence, square rods are the strong reflectors on a 2D plane, allowing the acoustic propagation to be dominated in the air media. A total reflection of the acoustic wave is considered due to high acoustic impedance mismatch between fluid and solid. Thus, waves prefer to get confined inside the lowest impedance region where the medium has low density and low longitudinal velocity.

It is known that the generation of a triply degenerated point at the center of Brillouin zone (BZ) or Γ point is the result of accidental degeneracy. A tunable engineered PnCs system is proposed [20], where multiple Dirac-like points can be generated at Γ point by tuning the orientation of the solid resonator. PVC rods with dimension $s = 0.342a$ and filling fraction = 0.1169, where a = lattice constant ≈ 25.4 mm, shown in Figure 1a are considered in this study. The first BZ (Figure 1b), which is the entire red square inside the supercell of Figure 1c, is reduced to a smaller region, Γ MX to be the irreducible BZ due to the lattice symmetry [26]. The acoustic dispersion curves are obtained along the periphery of the irreducible BZ (Γ MX) as shown in Figure 1d. Here, multiple regions are observed where a doubly degenerated mode and a single mode coexist. Two regions, named as “Dirac region A” (DRA) and “Dirac region B” (DRB) are selected for further tracking through tuning of the PnCs. It is to be noted that DRB is very close to a triply degenerated state, while DRA has apparent double degenerated state with a nearby single band with a partial BG between them. Therefore, to achieve DDC at two distinct energy states, a specific configuration of the PnCs, where both DRA and DRB are triply degenerated, needs to be found.

In this study, square PVC rods of infinite length are arranged in a square array. Initially, the rods have no rotation (i.e., $\theta = 0^\circ$) with respect to lattice orientation (Figure 1b). It is shown that with a careful tuning of the structure by rotating the lattices counterclockwise, the dispersion behavior helps to get triply degenerated at multiple frequencies at the Γ point (center of the BZ). Close observation of both the regions (DRA and DRB) reveals that the bands (red in Figure 2a), which are near-flat or parallel to the wave vector axis, are the “deaf bands”. The blue and the green bands are designated as T band (Top bands) and B band (Bottom bands), respectively. To prove the deafness of the deaf bands, the acoustic pressure mode shapes and the solid deformations of the PVC rods at DRA are presented in Figure 2a. With close observation, it is apparent from the mode shapes that the T and B bands are mutually orthogonal, with quadrupolar mode shapes. They hold proper symmetry with respect to the incident plane wave along Γ X [100] and Γ M [010] directions. However, both the deaf bands are antisymmetric with respect to the incident wave direction, lacking group velocity. In Figure 2b, the transmission study validates the deafness of the band, showing almost zero transmission near the deaf band. Thus, the deaf band remains inert to any kind of normal-incident plane wave due to antisymmetry. The concept of pivoting on the deaf bands and achieve Dirac-like cones at respective frequencies is a relatively new concept, and it is presented herein by performing a rotational tuning of the PnCs simultaneously at multiple frequencies.

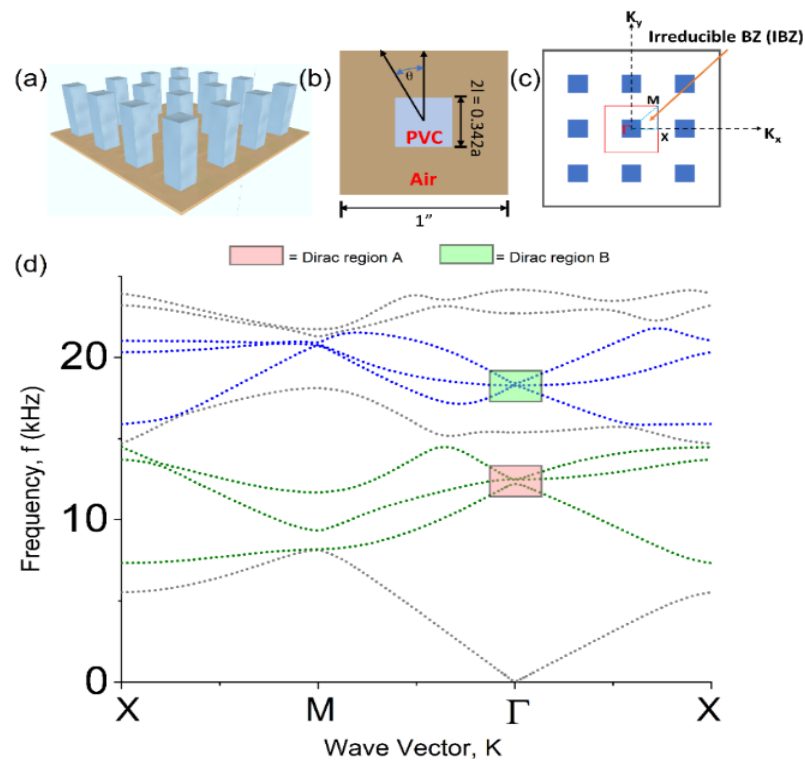


Figure 1. (a) Schematic representation of the two-dimensional periodic systems of hard square rods in a square lattice. The filling fraction is 0.1169 and the square array has the same orientation as the lattice, (b) Schematic view of the cross-section of the proposed PnC, composed of PVC having side, $2l = 0.342a$ hosted in air media, (c) transverse cross-section of the 2D square lattice of 3×3 supercell showing the irreducible Brillouin zone (Γ MX), two constituents are denoted by white and blue as air and PVC rods, respectively, (d) Acoustic band structure for PVC square rods of filling fraction, $F = 0.1169$ embedded in air host, rotational angle is $\theta = 0^\circ$. The colored regions along Γ denote probable Dirac region A and Dirac region B, having bands colored in green and blue, respectively.

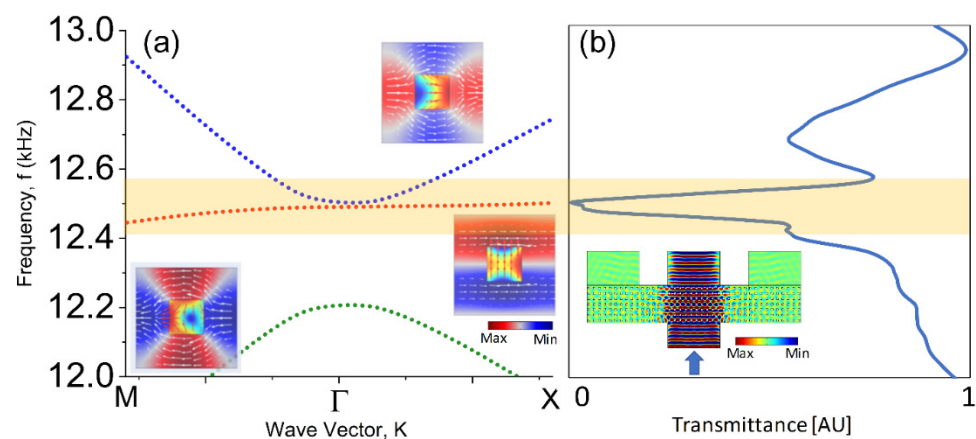


Figure 2. (a) The dispersion relation near DRA with the acoustic pressure mode distribution and solid displacement mode distribution of three of the bands near Γ point. The red band is termed as deaf band, (b) the deafness of the red deaf band is proved by the numerical calculation of the transmissibility study through a 40×7 cell of PVC/air matrix, showing almost zero transmission near the “deaf band”.

In Figure 3a, unit cells with different angular rotation of the PVC rod and their respective dispersion behavior are presented in a sequence. Only DRA and DRB areas are shown in Figure 3b with incremental angular tuning with increasing angle of rotation

(counterclockwise rotation). The B band at DRA experiences a significant alteration with respect to the energy state (frequency), whereas the doubly degenerated T band and the deaf band energy state remain approximately fixed with respect to the frequency axis. At $\theta = 9.7^\circ$, the counterclockwise angular rotation guarantees triple degenerated states at DRA forming a local linear dispersion. On the other hand, the DRB has very close triply degenerate state from the beginning ($\theta = 0^\circ$) and protects the triple degeneracy at $\theta = 9.7^\circ$. Hence, this establishes that two full triply degenerated points at the center of BZ are achieved with DRA and DRB at a tuning angle $\theta = 9.7^\circ$. In the literature, Quadro-degenerated points were reported before, where four bands intersected at a Dirac point, calling it a double Dirac-like cone [39,41,42]. However, in this case, six bands are involved in generating two Dirac cone locations at two distinct frequencies. Henceforth, this deaf band-based optimized formation of Dirac-like cone has been named as “Dual-Dirac-like cones” (DDC). Figure 4a,b presents both the Dirac-like cones (at $\theta = 9.7^\circ$) and present 3D equipfrequency surfaces (EFS) for B band, deaf band and T band, respectively (Figure 4(a1–a3,b1–b3)). Concentric circular shapes of EFSs indicate the existence of Dirac-like cones. With close observation, it is found that for both DRA and DRB with a tuning angle $\theta = 9.7^\circ$, the B band has a small but equal bandgap from the doubly degenerated state formed by a T band and the deaf band. It is found that to prevail Dirac cone behaviors, the above band structure is necessary, whereas the converse is not true. The converse occurs when the B band is degenerated with a deaf band, and the T band is lifted, leaving a bandgap.

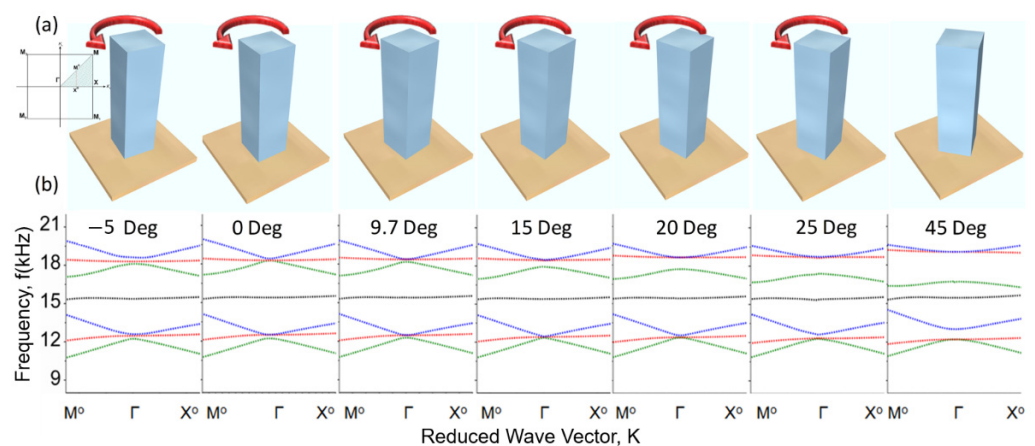


Figure 3. (a) Geometric representation of square rods rotated counterclockwise (CCW) at $\theta = -5^\circ, 0^\circ, 5^\circ, 9.7^\circ, 15^\circ, 20^\circ$ and 25° , embedded in air host. This angular tuning has been performed for the entire 90° CCW to demonstrate the Dual-Dirac phenomenon, among which only the above-mentioned are reported here, (b) The respective band structure dispersion relation for above-mentioned rotations for the rods, demonstrating the gradual process of undergoing triple degeneracy for DRA and DRB for $\theta = 9.7^\circ$, generating a Dual-Dirac phenomenon. Notably, both the deaf bands (red) remain almost fixed in position with respect to the frequency.

Furthermore, the existence of the Dirac-like points is confirmed by modeling a set of PnCs using COMSOL 4.3 Multiphysics simulation. The numerical frequency domain studies were conducted on a periodic structure made of square PnCS, rotated at an angle $\theta = 9.7^\circ$, as shown in Figure 5. In the numerical simulations, the PVC rods are assumed to be infinite in the third dimension, and the simulations are performed on a 2D plane to achieve fully converged results. Full 3D simulations are time consuming and are a limitation of numerical solutions.

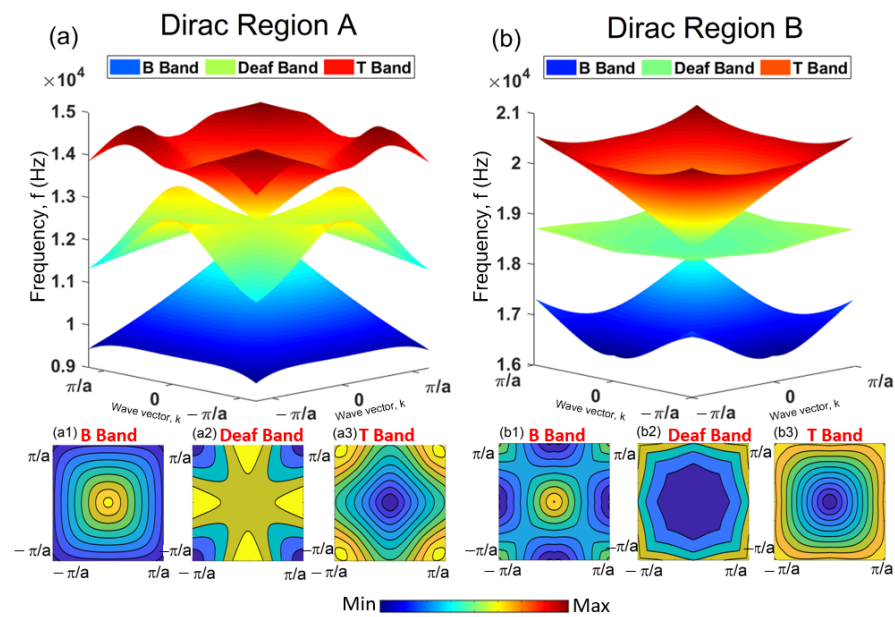


Figure 4. (a,b) depicts the equifrequency contours (EFC) for DRA and DRB while degenerated for $\theta = 9.7^\circ$, showing perfect triple degeneracy of Dirac cones at Γ of BZ. The equifrequency surfaces (EFS) or contour maps of acoustic band frequencies of three of the bands (T band, deaf band and B band, respectively) for both the regions displayed in the whole area of the first BZ are given in insets.

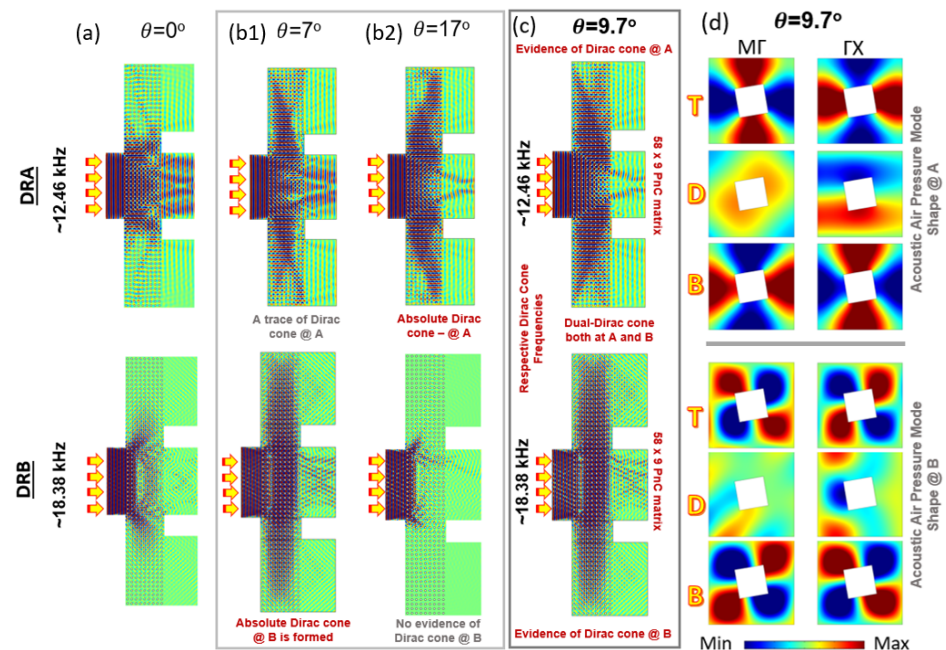


Figure 5. (a) Wave propagation and acoustic pressure distribution in a PnC guide with a 58×9 matrix of PVC/air media at DRA and DRB at excitation frequencies at the Dirac point $f = \sim 12.46$ kHz and $f = \sim 18.374$ kHz, respectively. The square PnCs are not rotated. (b1,b2) Wave propagation in the PnC guide at DRA and DRB at excitation frequencies at the Dirac points. The square PnCs are rotated at angles of 7° and 17° , respectively. DRB demonstrates Dirac phenomena at 7° , and DRA demonstrates Dirac phenomena at 17° . (c) Wave propagation in the PnC guide at DRA and DRB at excitation frequencies at the Dirac points. In this arrangement, the square PnCs are rotated at a 9.7° angle. Both frequencies demonstrate perfect Dirac phenomena. (d) Absolute acoustic pressure mode shapes of the unit cells in the $M\Gamma$ and ΓX directions for DRA and DRB, respectively, for the T, deaf and B bands when the PnCs are rotated at a 9.7° angle.

A periodic arrangement having 58×9 solid PVC square rods of filling fraction, $f = 0.1169$, are placed in the air medium. Acoustic pressure field distributions for both the DRA and DRB regions are presented in Figure 5. Acoustic pressure modes along ΓX and $M\Gamma$ for all the bands of DRA and DRB are shown in Figure 5 as well. The actuation of the periodic square PnCs was achieved by a guided plane wave source located at ~ 110 mm away from the air–PVC interface. A plane wave radiation boundary condition is assumed at all the boundaries to avoid unnecessary wave reflections. Triangular elements are selected for finite meshing of the simulation domain, with a maximum element size of $\lambda_{media}/10$, where λ_{media} is the acoustic wavelength at the maximum frequency 50 kHz. Orthogonal wave transportation at Dirac-like frequencies, can be visualized by making the arrangement portrayed in Figure 5a–c. Both Dirac regions demonstrate their respective unique features that are explained through wave-dispersion behavior below. The acoustic pressure distribution in the metastructure is shown in Figure 5a, where the PnCs are not rotated and regular arrangement of the square matrix at $\theta = 0^\circ$ is demonstrated. It shows no sign of Dirac phenomena on the grid. However, when the square PnCs on the grid are rotated together at an angle $\theta = 7^\circ$, as predicted, DRB at frequency ~ 18.38 kHz demonstrates absolute Dirac phenomena, shown in Figure 5(b1). DRA at frequency ~ 12.46 kHz also shows a trace of Dirac cone behavior [43], but it is not fully developed. When the square PnCs on the grid are rotated together at an angle $\theta = 17^\circ$, as predicted, DRA at frequency ~ 12.46 kHz demonstrates absolute Dirac phenomena, shown in Figure 5(b2). However, the Dirac behavior at DRB is totally dispersed. As the angle of rotation increases, DRB experiences a large separation/bandgap (Δf_{db}) between the B band and the doubly degenerated T and deaf bands. This is not the case for DRA when the rotational angle is $\theta = 7^\circ$. At DRA, Δf_{db} slowly changes due to the relative curvature of the B and deaf bands, as the angle of rotation changes between 7° and 17° . Guided by the Δf_{db} gap between the B and deaf bands at DRA and DRB, an equal gap of ~ 166 Hz is identified at $\theta = \sim 9.7^\circ$ where the Dirac phenomena predictively prevail. To prove this, a numerical experiment was conducted at both Dirac frequencies. The acoustic pressure distribution on the grid at DRA and DRB is shown in Figure 5c, when the PnCs are rotated together at an angle $\theta = 9.7^\circ$. The incident plane wave propagates in the actuation direction with no distortion at $f = 10$ kHz (not shown), but a drastic orthogonal bent line is demonstrated when the actuation frequency increases near the Dirac-like frequency for DRA ($f \sim 12.46$ kHz) and DRB ($f \sim 18.38$ kHz), as shown in Figure 5c. Minimal acoustic energy transmits in the actuation direction, forming an apparent bandgap. Keeping the phase shift at near zero, the plane wave travels along the PnCs orthogonally with respect to the actuation direction (Figure 5c). This establishes a prominent energy shift, producing a 45° bifurcation pattern. The wave-front bends another 90° toward the original actuation direction (ΓX), keeping the plane wave-front relatively intact. Due to its antisymmetry, the deaf band exhibits strong spatial localization and allows the wave-front to propagate orthogonally.

To further demonstrate the reason for the Dirac phenomena, the acoustic pressure mode shapes of the T, deaf and B bands for wave propagation along the ΓX and $M\Gamma$ directions at DRA and DRB frequencies are shown in Figure 5d. In both the DRA and DRB cases, the T and B band mode shapes are symmetric quadrupolar mode shapes with opposite pressure distributions. When the mode shapes are superposed at the Dirac frequencies, the T and B mode shapes cancel each other, causing the deaf band mode shape to dominate. The local dispersion behavior of the T and B bands with degenerated acoustic pressure mode shapes is quadrupolar and mutually orthogonal; in contrast, the deaf band mode is dipolar (for ΓX) (Figure 5d). Hence, at the Dirac frequency, both the T and B bands nullify each other, maintaining the dipolar deaf band mode dominance. A 45° bent line helps the dipolar deaf mode carry the wave energy orthogonally like origami. The T and B bands' quadrupolar local dispersion modes rotate by 90° between the $M\Gamma$ and ΓX directions of propagation at both DRA and DRB (Figure 5d) frequencies. To summarize, there are other scenarios where flat bands are achieved. They are due to the local resonance

of the PnCs and yield zero-group velocity. Although the deaf band is almost flat, the phenomenon inside the material is not due to the local resonance but due to antisymmetric mode shape at the triple degenerated state, as depicted in Figure 5.

The transmissibility study in Figure 6 at DRA with $\theta = 9.7^\circ$ shows the drop-in transmission approximately to zero along ΓX direction, while the transmission remains maximum along the orthogonal (XM) direction.

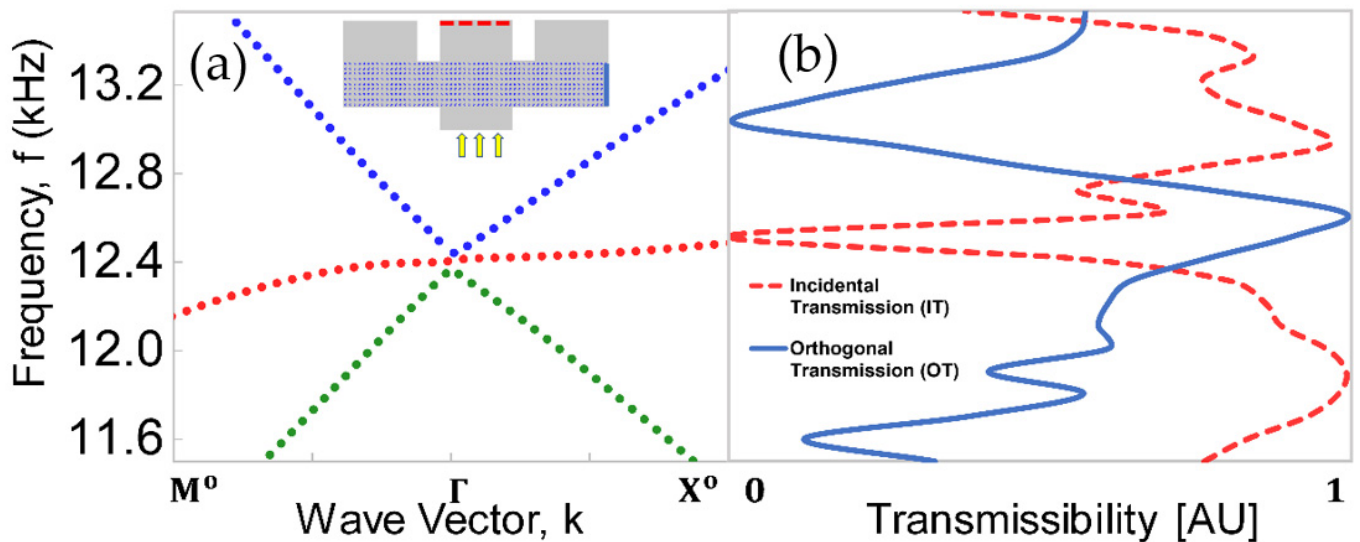


Figure 6. (a) The zoomed in band dispersion relation at DRA for $\theta = 9.7^\circ$ calculated numerically, (b) a comparison of the numerical results of acoustic transmission (normalized) excited along the ΓX direction with DRA frequencies. The peak transmission is seen at the Dirac-like frequency along the orthogonal direction (OT—blue) shown in the PnCs arrangement in inset, while the transmission dip is observed along the actuation direction (IT—red) for that respective frequency, validating the phenomenon realized in Figure 5.

Spatial phase reconstruction due to excitation of an accidentally degenerated Bloch mode at the high symmetry Γ point is reported and discussed in photonics. Utilizing such property, an acoustic cloaking phenomenon can also be demonstrated in phononics with a near-flat band (deaf band) around Γ point of the Brillouin zone. Acoustic cloaking has already drawn some attention over the past few years [44–47]. As shown in Figure 7, a $75 \text{ mm} \times 75 \text{ mm}$ square steel (AISI 4340) block is embedded in the middle of the PnCs ribbon having 20×15 array of PnCs in air media. This square steel block is chosen as an object to be cloaked. The plane wave source is placed approximately 127 mm away from the left interface of the air–PVC PnCs ribbon. Three different combinations are used to demonstrate the acoustic cloaking. The first one is without any square steel block (Figure 7(a1,a2)) and the second one is with a square steel block. Both configurations experience plane wave incidence. The third combination is with a square steel block experiencing a tightly focused Gaussian beam incidence. Next, the configurations are excited at two different frequencies: one at 10 kHz and the other at Dirac frequency of DRA which is $\sim 12.458 \text{ kHz}$. From Figure 7(a1,a2), the orthogonal wave transportation is observed without any cloaking object inside the PnCs. From Figure 7(b2), it is evident that the acoustic wave could transmit through the PnCs as if the square steel block were absent, as the planar wave-front of the transmitted acoustic wave remains undistorted inside the PnCs, whereas the plane-wave distorts significantly when excited at the frequency (10 kHz) (Figure 7(b1)). Similarly, when a focused Gaussian beam is excited at Dirac frequency, the cloaking phenomena persist (Figure 7(c2)). However, if the PnCs are removed, then the planar wave-front of the incident acoustic wave gets severely distorted by the steel block, indicating the absence of the cloaking effect.

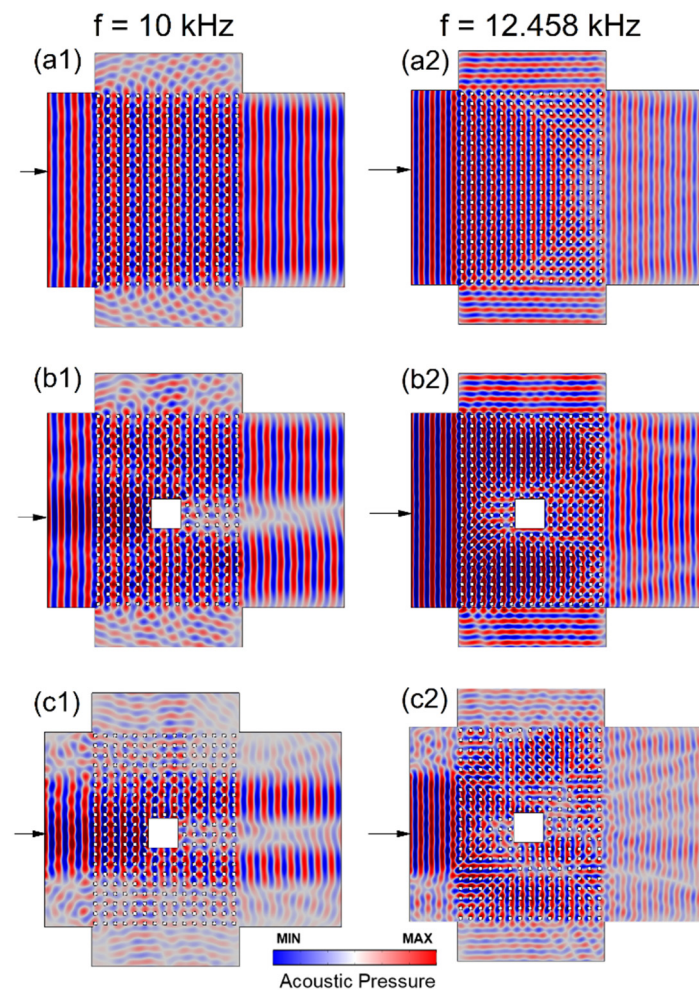


Figure 7. Simulation results showing the absolute pressure field distribution where waves can pass through a waveguide with an embedded obstacle, (a1,a2) The case where no square steel rod is inserted into the middle of the PnCs slab, and the incident plane wave frequencies are 10 kHz and 12.458 kHz, respectively, (b1,b2) The same case as that shown in (a1,a2), except that we inserted a square steel block to be cloaked, (c1,c2) a similar case here, except that a Gaussian incident beams were used here instead of plane wave for similar frequencies. The steel block has been perfectly cloaked at Dirac frequency for DRA keeping the planar wave-front intact, while the wave-front distorts severely for actuation frequency below Dirac frequency, $f = 10$ kHz.

Apart from the acoustic cloaking effect, a spatial phase reconstruction along with wave-front reshaping, pseudo-diffusion and acoustic collimation have been studied in the past few years [48–50]. Absolute acoustic pressure field distributions are demonstrated for both incident circular waves, Gaussian waves and plane waves, respectively. First, the normalized pressure field distributions are shown at different frequencies, including Dirac frequency, from a circular-crested wave source. Studies were conducted when the PnCs were absent. Similarly, when a block of (28×13) grid rotated PnCs rotated at an angle 9.7° arranged along the Γ -K direction, the circular wave was again excited at the Dirac frequency. Figure 8(a1) shows that in the absence of any periodic square PnCs at the Dirac frequency (12.458 kHz), the circular wave-front maintains the phases and the wave shape without any distortion. However, once the rotated PnCs are placed inside the air media, the propagation of the circular wave-front at that Dirac frequency (12.458 kHz) exhibits ballistic wave transmission with a collimated plane wave traveling mostly along Γ -X direction (Figure 8(a2)). This ballistic feature is identical to the one that is observed in a beam of fixed-width propagates without changing the beam width. Next, the acoustic

wave transmission inside a 20×15 PnCs arranged with Dirac rotation of 9.7° is studied when a Gaussian wave ($\mu = 0$ and $\sigma = 2.5 \times 10^3$) is excited along the Γ -X direction at a frequency of 10 kHz. The incident wave amplitude across the actuator's width varies using a Gaussian function. The Gaussian wave input transforms into a planar wave output with equal amplitudes along the planar wave-front due to the presence of the PnCs (Figure 8(b1)). However, when the actuation frequency increases to 12.458 kHz, wave diffusion occurs, creating planar wave-fronts through all three outlets, as shown in Figure 8(b2). Surprisingly, when the smaller number of PnCs are used in the guide, wave diffusion not only happens along the orthogonal direction, but wave diffuses with planar wave-front in the incident direction. Orthogonal wave transport prevails even above ~ 12.46 kHz up to ~ 13 kHz. This is in contrast to Figure 6 obtained from a matrix of 40×7 elements. Hence, the presence of the number of PnCs along the orthogonal to the incident wave plays a vital role in reconstructing the phase to form collimated plane waves and wave diffusion. This may have practical applications in engineering and biomedical science when waves are required to predictively guide in fluid and solid media. Similar scenario with planar wave incident is shown in Figure 8(c1,c2) on a comparatively smaller setup with 10×10 PnCs, suitable for performing a laboratory experiment (not presented in this article).

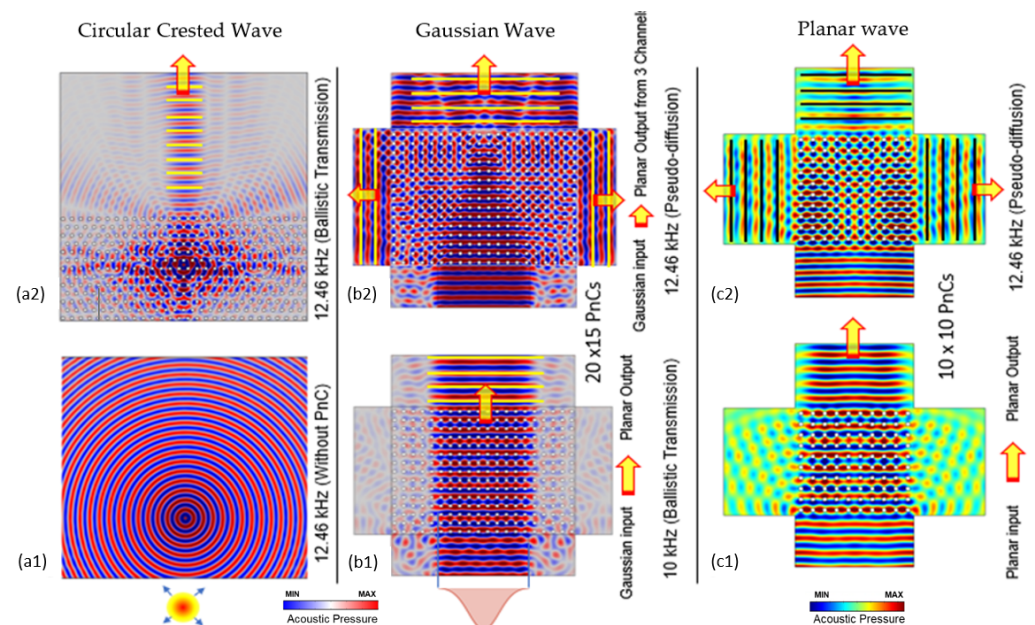


Figure 8. (a1) Pressure field distribution for cylindrical wave excited by a pseudo-point source at Dirac frequency, without any PnCs ribbon, (a2) a prominent ballistic transmission along Γ X when the square rod PnCs were introduced, at $f = 12.458$ kHz, A PnCs ribbon with a 28×13 matrix acting as a perfect acoustic collimator, diffuser, and a wave-front reshaping media excited around the Dirac frequency, while excited by a pseudo-point source inside the PnCs, (b1) Pressure field distribution when a Gaussian beam is incident on PnCs slab at $f = 11$ kHz, depicting perfect ballistic transmission, (b2) A Gaussian wave source is excited at the Dirac frequency. Wave diffusion due to orthogonal transport is eminent and wave-front transformation from Gaussian beam to plane wave-front is observed at $f = 12.458$ kHz (c1) A planar wave source is excited at frequencies below the Dirac frequency, output wave transmission is planar wave, (c2) A planar wave source is excited at the Dirac frequency. Wave diffusion due to orthogonal transport is eminent.

4. Conclusions

This study proposed deaf band-based angular tuning to generate multiple triple degeneracies (Dirac cones) at the center of the BZ. The predictive optimization process discussed in this article demonstrated the possibility of creating DDC. Dirac cones were achieved near the region where near zero-group velocity flat or deaf bands existed. By

maintaining the same filling fraction and without replacing the crystal, deaf band-based angular tuning was accomplished, yielding multiple degenerated regions. The widening of the dispersion bands was maximized or minimized, modulating the deaf band and demonstrating the Dual-Dirac-like phenomenon.

Section 2:

- An analytical approach to solve the eigenvalue problem of a square rod in a fluid media is presented.

Section 3:

- Wave transmission behavior through wave guides made of square PnCs was studied numerically by calculating the absolute acoustic pressure field using finite element analysis software.
- Different acoustic application-based phenomena that occurred at Dirac-like points, such as acoustic orthogonal transportation, acoustic phase reconstruction and acoustic collimation, including ballistic transmission and pseudo-diffusion, were studied and realized using the proposed numerical model.
- Acoustic cloaking and effects on wave-front reshaping were demonstrated. PnCs provide an intriguing platform to explore acoustic condensed matter physics regarding Dirac-like cones at Γ point in acoustic wave systems.

In conclusion, the achievement of DDC proposed herein increases the possibility of exploiting numerous Dirac point behaviors at different frequencies in a single lattice structure. A specific band structure is responsible for demonstrating such phenomena. While deaf band-based tuning is designed, it must look for a top band degenerated with a deaf band when a bottom band is lifted, leaving a small bandgap. Such scenario will help track the deaf band frequency to form a Dirac-like cone. This may provide greater design flexibility for practical wave manipulation. It is anticipated that this study will encourage further numerical and experimental investigations into band degeneracies for extensive acoustic device applications.

Author Contributions: Conceptualization, S.B.; methodology, M.M.I.; software, M.M.I.; validation, M.M.I. and S.B.; formal analysis, M.M.I.; investigation, S.B. and M.M.I.; resources, S.B.; data curation, M.M.I.; writing—original draft preparation, M.M.I.; writing—review and editing, S.B.; visualization, M.M.I. and S.B.; supervision, S.B.; project administration, S.B.; funding acquisition, S.B. All authors have read and agreed to the published version of the manuscript.

Funding: This research was partially funded by NASA Langley Research Center (LaRC) under Contract No. NNL15AA16C and USDA NIFA Grant No. 2017-67017-26167.

Institutional Review Board Statement: Not applicable.

Informed Consent Statement: Not applicable.

Data Availability Statement: The data presented in this study are available on request from the corresponding author. The data are not publicly available due to further continuing research.

Conflicts of Interest: The authors declare no conflict of interest.

Nomenclature

PnC	Phononic Crystals
BZ	Brillouin Zone
QVHE	Quantum Valley Hall Effect
PWE	Plane Wave Expansion
PVC	Polyvinyl Chloride
DRA	Dirac Region A
DRB	Dirac Region B
DDC	Dual-Dirac-like Cones

References

1. Kushwaha, M.S.; Halevi, P.; Dobrzynski, L.; Djafari-Rouhani, B. Acoustic band structure of periodic elastic composites. *Phys. Rev. Lett.* **1993**, *71*, 2022–2025. [[CrossRef](#)]
2. Kushwaha, M.S.; Halevi, P.; Martínez, G.; Dobrzynski, L.; Djafari-Rouhani, B. Theory of acoustic band structure of periodic elastic composites. *Phys. Rev. B* **1994**, *49*, 2313–2322. [[CrossRef](#)] [[PubMed](#)]
3. Sigalas, M.M.; Economou, E. Attenuation of multiple-scattered sound. *Europhys. Lett.* **1996**, *36*, 241–246. [[CrossRef](#)]
4. Vasseur, J.; A Deymier, P.; Frantziskonis, G.; Hong, G.; Djafari-Rouhani, B.; Dobrzynski, L. Experimental evidence for the existence of absolute acoustic band gaps in two-dimensional periodic composite media. *J. Phys. Condens. Matter* **1998**, *10*, 6051–6064. [[CrossRef](#)]
5. Liu, Z.; Chan, C.T.; Sheng, P.; Goertzen, A.; Page, J. Elastic wave scattering by periodic structures of spherical objects: Theory and experiment. *Phys. Rev. B* **2000**, *62*, 2446–2457. [[CrossRef](#)]
6. Liu, Z.; Zhang, X.; Mao, Y.; Zhu, Y.Y.; Yang, Z.; Chan, C.T.; Sheng, P. Locally Resonant Sonic Materials. *Science* **2000**, *289*, 1734–1736. [[CrossRef](#)] [[PubMed](#)]
7. Sun, X.-C.; He, C.; Liu, X.-P.; Zou, Y.; Lu, M.-H.; Hu, X.; Chen, Y.-F. Photonic Topological States in a Two-Dimensional Gyrotropic Photonic Crystal. *Crystals* **2019**, *9*, 137. [[CrossRef](#)]
8. Li, X.; Wu, F.; Hu, H.; Zhong, S.; Liu, Y. Large acoustic band gaps created by rotating square rods in two-dimensional periodic composites. *J. Phys. D Appl. Phys.* **2002**, *36*, L15. [[CrossRef](#)]
9. Wu, F.; Liu, Z.; Liu, Y. Acoustic band gaps created by rotating square rods in a two-dimensional lattice. *Phys. Rev. E* **2002**, *66*, 046628. [[CrossRef](#)]
10. Wu, F.; Zhong, H.; Zhong, S.; Liu, Z.; Liu, Y. Localized states of acoustic waves in three-dimensional periodic composites with point defects. *Eur. Phys. J. B* **2003**, *34*, 265–268. [[CrossRef](#)]
11. Anderson, C.M.; Giapis, K.P. Larger two-dimensional photonic band gaps. *Phys. Rev. Lett.* **1996**, *77*, 2949. [[CrossRef](#)] [[PubMed](#)]
12. Anderson, C.M.; Giapis, K.P. Symmetry reduction in group 4mm photonic crystals. *Phys. Rev. B* **1997**, *56*, 7313. [[CrossRef](#)]
13. Caballero, D.; Sanchez-Dehesa, J.; Rubio, C.; Martinez-Sala, R.; Sanchez-Perez, J.; Meseguer, F.; Llinares, J. Large two-dimensional sonic band gaps. *Phys. Rev. E* **1999**, *60*, R6316. [[CrossRef](#)] [[PubMed](#)]
14. Zhang, X.; Zhang, Z.-Q.; Li, L.-M.; Jin, C.; Zhang, D.; Man, B.; Cheng, B. Enlarging a photonic band gap by using insertion. *Phys. Rev. B* **2000**, *61*, 1892. [[CrossRef](#)]
15. Jo, S.-H.; Youn, B.D. A Phononic Crystal with Differently Configured Double Defects for Broadband Elastic Wave Energy Localization and Harvesting. *Crystals* **2021**, *11*, 643. [[CrossRef](#)]
16. Yang, M.; Ran, X.-J.; Cui, Y.; Wang, R.-Q. Quantum Hall-like effect in gated four-terminal graphene devices without magnetic field. *Appl. Phys. Lett.* **2011**, *99*, 222101. [[CrossRef](#)]
17. Yang, L.; Yu, K.; Wu, Y.; Zhao, R.; Liu, S. Topological spin-Hall edge states of flexural wave in perforated metamaterial plates. *J. Phys. D Appl. Phys.* **2018**, *51*, 325302. [[CrossRef](#)]
18. Ochiai, T.; Onoda, M. Photonic analog of graphene model and its extension: Dirac cone, symmetry, and edge states. *Phys. Rev. B* **2009**, *80*, 155103. [[CrossRef](#)]
19. Karsenty, A. A Comprehensive Review of Integrated Hall Effects in Macro-, Micro-, Nanoscales, and Quantum Devices. *Sensors* **2020**, *20*, 4163. [[CrossRef](#)]
20. Goffaux, C.; Vigneron, J.P. Theoretical study of a tunable phononic band gap system. *Phys. Rev. B* **2001**, *64*, 075118. [[CrossRef](#)]
21. Lai, Y.; Zhang, X.; Zhang, Z.-Q. Large sonic band gaps in 12-fold quasicrystals. *J. Appl. Phys.* **2002**, *91*, 6191–6193. [[CrossRef](#)]
22. Vasseur, J.; Deymier, P.A.; Khelif, A.; Lambin, P.; Djafari-Rouhani, B.; Akjouj, A.; Dobrzynski, L.; Fettouhi, N.; Zemmouri, J. Phononic crystal with low filling fraction and absolute acoustic band gap in the audible frequency range: A theoretical and experimental study. *Phys. Rev. E* **2002**, *65*, 056608. [[CrossRef](#)] [[PubMed](#)]
23. Susa, N. Large absolute and polarization-independent photonic band gaps for various lattice structures and rod shapes. *J. Appl. Phys.* **2002**, *91*, 3501–3510. [[CrossRef](#)]
24. Wu, F.; Liu, Z.; Liu, Y. Splitting and tuning characteristics of the point defect modes in two-dimensional phononic crystals. *Phys. Rev. E* **2004**, *69*, 066609. [[CrossRef](#)]
25. Zhong, L.; Wu, F.; Zhang, X.; Zhong, H.; Zhong, S. Effects of orientation and symmetry of rods on the complete acoustic band gap in two-dimensional periodic solid/gas systems. *Phys. Lett. A* **2005**, *339*, 164–170. [[CrossRef](#)]
26. Dong, H.; Wu, F.; Zhong, H.; Zhang, X.; Yao, Y. Effects of asymmetrical rotated rectangular basis on the acoustic band gap in two-dimensional acoustic crystals: The bands are twisted. *J. Phys. D Appl. Phys.* **2010**, *43*, 105404. [[CrossRef](#)]
27. Zhao, H.; Liu, R.; Shi, C.; Guo, H.; Deng, Z. Effects of rotated square inserts on the longitudinal vibration band gaps in thin phononic crystal plates. *Mod. Phys. Lett. B* **2015**, *29*, 1550105. [[CrossRef](#)]
28. Song, A.; Wang, X.; Chen, T.; Wan, L. Band structures in a two-dimensional phononic crystal with rotational multiple scatterers. *Int. J. Mod. Phys. B* **2017**, *31*, 1750038. [[CrossRef](#)]
29. Hyun, J.; Choi, W.; Wang, S.; Park, C.-S.; Kim, M. Systematic realization of double-zero-index phononic crystals with hard inclusions. *Sci. Rep.* **2018**, *8*, 7288. [[CrossRef](#)] [[PubMed](#)]
30. Indaleeb, M.M.; Banerjee, S.; Ahmed, H.; Saadatzi, M.; Ahmed, R.J.P.R.B. Deaf band based engineered Dirac cone in a periodic acoustic metamaterial: A numerical and experimental study. *Phys. Rev. B* **2019**, *99*, 024311. [[CrossRef](#)]

31. Robertson, W.; Arjavalingham, G.; Meade, R.; Brommer, K.; Rappe, A.M.; Joannopoulos, J. Measurement of photonic band structure in a two-dimensional periodic dielectric array. *Phys. Rev. Lett.* **1992**, *68*, 2023. [[CrossRef](#)] [[PubMed](#)]
32. Sánchez-Pérez, J.V.; Caballero, D.; Martínez-Sala, R.; Rubio, C.; Sánchez-Dehesa, J.; Meseguer, F.; Linares, J.; Gálvez, F. Sound attenuation by a two-dimensional array of rigid cylinders. *Phys. Rev. Lett.* **1998**, *80*, 5325. [[CrossRef](#)]
33. Psarobas, I.; Modinos, A.; Sainidou, R.; Stefanou, N. Acoustic properties of colloidal crystals. *Phys. Rev. B* **2002**, *65*, 064307. [[CrossRef](#)]
34. Li, J.; Chan, C.T. Double-negative acoustic metamaterial. *Phys. Rev. E* **2004**, *70*, 055602. [[CrossRef](#)] [[PubMed](#)]
35. Hsiao, F.-L.; Khelif, A.; Moubchir, H.; Choujaa, A.; Chen, C.-C.; Laude, V. Complete band gaps and deaf bands of triangular and honeycomb water-steel phononic crystals. *J. Appl. Phys.* **2007**, *101*, 044903. [[CrossRef](#)]
36. Sigalas, M.; Economou, E.N. Band structure of elastic waves in two dimensional systems. *Solid State Commun.* **1993**, *86*, 141–143. [[CrossRef](#)]
37. Tanaka, Y.; Tomoyasu, Y.; Tamura, S.-I. Band structure of acoustic waves in phononic lattices: Two-dimensional composites with large acoustic mismatch. *Phys. Rev. B* **2000**, *62*, 7387. [[CrossRef](#)]
38. Shelke, A.; Banerjee, S.; Habib, A.; Rahani, E.K.; Ahmed, R.; Kundu, T. Wave guiding and wave modulation using phononic crystal defects. *J. Intell. Mater. Syst. Struct.* **2014**, *25*, 1541–1552. [[CrossRef](#)]
39. Chen, Z.-G.; Ni, X.; Wu, Y.; He, C.; Sun, X.-C.; Zheng, L.-Y.; Lu, M.-H.; Chen, Y.-F. Accidental degeneracy of double Dirac cones in a phononic crystal. *Sci. Rep.* **2014**, *4*, 4613. [[CrossRef](#)] [[PubMed](#)]
40. Fugen, W.; Zhengyou, L.; Youyan, L. Acoustic band gaps in 2D liquid phononic crystals of rectangular structure. *J. Phys. D Appl. Phys.* **2002**, *35*, 162.
41. Li, Y.; Mei, J. Double Dirac cones in two-dimensional dielectric photonic crystals. *Opt. Express* **2015**, *23*, 12089–12099. [[CrossRef](#)]
42. Kim, S.-H.; Kim, S.; Kee, C.-S. Photonic crystals composed of virtual pillars with magnetic walls: Photonic band gaps and double Dirac cones. *Phys. Rev. B* **2016**, *94*, 085118. [[CrossRef](#)]
43. Indaleeb, M.M.; Ahmed, H.; Saadatzi, M.; Banerjee, S. Deaf band-based prediction of Dirac cone in acoustic metamaterials. *J. Appl. Phys.* **2020**, *127*, 064903. [[CrossRef](#)]
44. Hao, J.; Yan, W.; Qiu, M. Super-reflection and cloaking based on zero index metamaterial. *Appl. Phys. Lett.* **2010**, *96*, 101109. [[CrossRef](#)]
45. Popa, B.-I.; Zigoneanu, L.; Cummer, S.A. Experimental Acoustic Ground Cloak in Air. *Phys. Rev. Lett.* **2011**, *106*, 253901. [[CrossRef](#)] [[PubMed](#)]
46. Zhu, X.; Liang, B.; Kan, W.; Zou, X.; Cheng, J. Acoustic Cloaking by a Superlens with Single-Negative Materials. *Phys. Rev. Lett.* **2011**, *106*, 014301. [[CrossRef](#)]
47. Zheng, L.-Y.; Wu, Y.; Ni, X.; Chen, Z.-G.; Lu, M.-H.; Chen, Y.-F. Acoustic cloaking by a near-zero-index phononic crystal. *Appl. Phys. Lett.* **2014**, *104*, 161904. [[CrossRef](#)]
48. Chan, C.T.; Hang, Z.H.; Huang, X. Dirac Dispersion in Two-Dimensional Photonic Crystals. *Adv. Optoelectron.* **2012**, *2012*, 11. [[CrossRef](#)]
49. Lu, J.; Qiu, C.; Xu, S.; Ye, Y.; Ke, M.; Liu, Z. Dirac cones in two-dimensional artificial crystals for classical waves. *Phys. Rev. B* **2014**, *89*, 134302. [[CrossRef](#)]
50. Yu, S.-Y.; Wang, Q.; Zheng, L.-Y.; He, C.; Liu, X.-P.; Lu, M.-H.; Chen, Y.-F. J.A.P.L. Acoustic phase-reconstruction near the Dirac point of a triangular phononic crystal. *Appl. Phys. Lett.* **2015**, *106*, 151906. [[CrossRef](#)]